PHYSICAL REVIEW B **70**, 125102 (2004)

Infrared and Raman evidence for the charge-ordering in β''-(BEDT-TTF)$_3$(ReO$_4$)$_2$

Takashi Yamamoto,* Mikio Uruichi, and Kyuya Yakushi
Institute of Molecular Science, Myodaiji, Okazaki, 444-8585, Japan

Jun-ich Yamaura and Hiroyuki Tajima
Institute for Solid State Physics, University of Tokyo, Kashiwnoha, Kashiwa, 277-8581, Japan

(Received 29 October 2003; revised manuscript received 17 February 2004; published 8 September 2004)

We present the infrared and Raman spectra of β''-(BEDT-TTF)$_3$(ReO$_4$)$_2$ (BEDT-TTF=bis-ethylenedithio-tetrathiafulvalene) measured at various temperatures. We investigated the three C═C stretching modes, ν_2, ν_{27}, and ν_3. The infrared and Raman spectra discontinuously changed at 80 K. Below 80 K, for example, the doublet ν_2 bands split into three peaks, the doublet ν_{27} also split into three, and a mutual exclusion rule for the vibronic ν_3 modes in the infrared and Raman spectra was broken. This symmetry lowering was consistent with the result of x-ray crystal structure analyses conducted at 100 K and 22 K. The site charges in the unit cell estimated from the splitting of ν_2 were $+0.7_3, +0.7_3$, and $+0.5_3$ in the metallic phase, and they were $+0.2$, $+0.8_5$, and $+0.9_5$ in the insulating phase. The metal-insulator transition of this compound was characterized as the charge-ordering transition originated from the localization of charge due to Coulomb interactions.

DOI: 10.1103/PhysRevB.70.125102 PACS number(s): 78.30.−j, 71.30.+h

I. INTRODUCTION

Low-dimensional molecular conductors have demonstrated a variety of ground states such as charge-density wave (CDW), spin-density wave (SDW), superconducting (SC), antiferromagnetic states, etc.[1] Numerous studies have been devoted to κ-type BEDT-TTF salts (EDT-TTF=bis-ethylenedithio-tetrathiafulvalene, hereafter BEDT-TTF is further abbreviated to ET) to investigate the electronic phase diagram. Since ET molecules in κ-salts form a strong dimer,[2] κ-salts can be regarded as a half-filled system, and therefore the insulating state is regarded as a Mott insulator.[3] However, there has been no general understanding for the mechanism of the metal-insulator transition of various ET salts that has no dimerized structure. Recently, the charge-ordering (CO) state has received an attention in order to understand the insulating state of the nondimerized system, such as θ-(ET)$_2$RbZn(SCN)$_4$ (Refs. 4–6) and α-(ET)$_2$I$_3$ (Ref. 7). In this case, the intersite Coulomb interaction participates in the insulating mechanism in addition to the on-site Coulomb interaction. Among various nondimerized ET salts, the β''-salts has attracted strong attention, since Merino and McKenzie predicted that some metallic β''-salts fall into the CO state close to a SC state with a new SC mechanism different from that in κ-salts.[8] However, there has been no experimental study to verify the CO state in the β''-salts, to our best knowledge. As the first step for understanding the phase diagram of β''-salt, we focus on β''-(ET)$_3$(ReO$_4$)$_2$, because this family has the simplest structure—three ET molecules are accommodated in a conducting layer of a unit cell.[9,10] Carneiro *et al.* found a magnetic phase transition at T_c=88 K, below which the ESR intensity showed an activationlike decrease and the ESR signal split into two.[11] This magnetic transition was interpreted as a Peierls transition.[11] Parkin *et al.* reported the metal-insulator transition in the resistivity of β''-(ET)$_3$(ReO$_4$)$_2$ at around 100 K.[12] They pointed out the important role of the interstack interaction, and they excluded the simple one-dimensional model. Yakushi *et al.* reported the reflectivity and resistivity.[13] The reflectivity exhibited a two-dimensional nature of the band structure. Using the tight-binding calculation, they provided a two-dimensional semimetallic band for this compound. The resistivity changed the sign of dR/dT rather continuously in the temperature range of 130–170 K and steeply increased below ~85 K.[13] By contrast, the reflectivity showed a discontinuous change with a hysteresis (at 83 K on cooling and at 88 K on heating runs).[13] They speculated that the opening of gap came from the disappearance of the electron and hole pockets caused by a small structural change.[13] However, the mechanism of the metal-insulator transition of this compound has not been established still now. Recently, Baker *et al.* reported the optical conductivity in the far-infrared region, which showed no Drude response down to 40 cm^{-1} in the metallic state at 300 K.[14] This result implies that Coulomb interactions have a strong influence on the dynamics of the charge carriers at 300 K. Therefore, we investigate the metal-insulator transition of β''-(ET)$_3$(ReO$_4$)$_2$ from the viewpoint of the charge localization caused by Coulomb interactions. It has been demonstrated that the C═C stretching modes of ET sensitively reflect the charge distribution in the unit cell.[5] In this paper, we used the method of infrared and Raman spectroscopy focusing on the spectral region of the C═C stretching modes, ν_2, ν_{27}, and ν_3, which are schematically shown in Fig. 1. In order to examine the structural change near the metal-insulator phase transition, we conducted the x-ray crystal structure analyses at 300 K, 100 K, and 22 K.

II. EXPERIMENTAL METHODS

Single crystals were synthesized by a galvanostatic method in THF [=tetrahydrofuran]. The largest crystal face corresponds to the crystallographic *ac* plane. After growing single crystals for longer than 4 weeks, thick crystals were

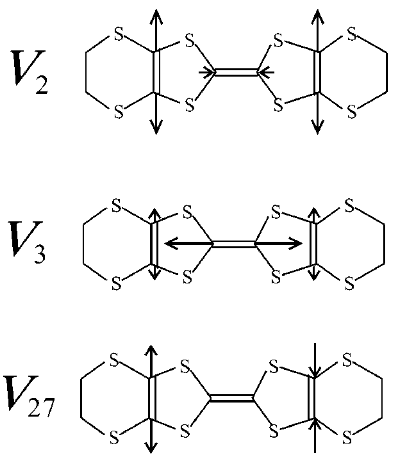

FIG. 1. Schematic views of three fundamental C═C stretching modes of ET molecule.

obtained. A typical dimension for the reflectivity measurement was $5\times3\times0.5$ mm. In this size of crystal, we were able to obtain a good quality of polarized reflectance spectra along the *b* direction.

Raman spectra were measured on a Renishaw Ramascope system-1000 with backward-scattering configuration. The system is composed of a microscope, couple of notch filters, spectrometer, and CCD detector. Single crystals were excited by He-Ne laser (632.6 nm), by Ar^+ laser (514.5 nm) and by diode laser (780 nm). By use of appropriate ND(=neutral density) filters, the intensity of the excitation light was reduced to less than 0.1 mW. The irradiated area was $\sim5\times5$ μm. In this range of light intensity, no damage on a sample surface was observed throughout the experiments. The frequency corrections of the measurement system were made based on the TO mode of a diamond (1332 cm^{-1}) and on the emission of a Ne lamp. The resolution of the spectrometer was 2 cm^{-1}. All the Raman spectra were measured using the polarizations of $a(c^*c^*)a$, $a(bc^*)a$, $a(bb)a, b(aa)b$, $b(ac^*)b, b(cc)b, c(a^*a^*)c, c(a^*b)c$, and $c(bb)c$. Here, $u(xy)v$ denotes the experimental condition: u and v give the directions of the incident and scattered light; x and y give the directions of the corresponding polarizations. The grating in the spectrometer has difference in the spectral sensitivity for parallel and perpendicular polarized light. In order to obtain the spectra in the $u(xx)u$ geometry (diagonal component), a polarizer was placed between microscope and spectrometer. In order to obtain the spectra in the $u(xy)u$ geometry (off-diagonal component), we placed the $\lambda/2$ plate between the excitation laser and microscope. By use of these optical systems, we were able to avoid the difference in the sensitivity from spectrometer. The measurement times were 60 and 90 minutes for the diagonal and off-diagonal components, respectively. The single crystal for the Raman spectra was cooled using a continuous-flow helium cryostat manufactured at Oxford Instruments (CF1104s). The cooling rate was kept within 0.3 K/min.

Polarized reflectance spectra were observed by use of a Nicolet Magna 760 FT-IR spectrometer and a Spectrotech IR-Plan microscope. The spectral resolution was 4 cm^{-1}. Incident lights were polarized along the crystallographic *b* and [102] directions. A number of collecting scans were 5×100 times. We used the similar cryostat as that for the Raman experiment. Optical conductivity $\sigma(\omega)$ was obtained through a Kramer-Kronig transformation.

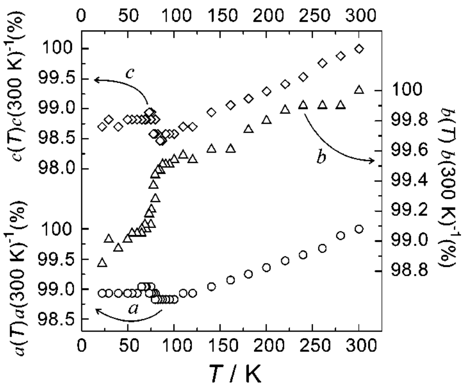

FIG. 2. Temperature dependence of the lattice constants.

X-ray diffraction data were collected on an imaging-plate type Weissenberg camera (Mac Science DIP320V) with graphite-monochromated Mo Kα radiation. The size of single crystal for the measurement was 10 mm$\times$3 mm $\times$0.3 mm. The single crystal was cooled by helium-gas flow. The measurement temperatures were 300 K, 100 K, and 22 K. The crystal structure was solved by a direct method and refined by using the SHELXL97 package.[15]

III. EXPERIMENTAL RESULTS

A. Structural change in the phase transition

Figure 2 shows the temperature dependences of the lattice constants. The data points were normalized against those of 300 K. With decreasing temperature down to ~80 K, a, b, and c exhibited continuous thermal contraction. The b axis exhibited a discontinuous contraction at around 80 K. The lattice constants (a and c) in the organic layer also showed a subtle and discontinuous jump at around 80 K. Below 80 K, a and c were almost leveled off. Table I shows the crystallographic data obtained at 300, 100, and 22 K. The result at 300 K is in agreement with that in Ref. 16. Figures 3(a) and 3(b) show the molecular arrangements in the conducting layers at 100 K and 22 K, respectively. The structure at 100 K was successfully solved on the assumption that the space group is $P2_1/n$, which was the same space group at 300 K. As described in Ref. 16, the molecule I was located on the inversion center, and the molecules II located on the general positions were related to each other by the inversion center. The ethylene end groups at site I had a staggered conformation, whereas those at site II had an eclipsed conformation. The structure at 22 K was successfully solved on the assumption that the space group is $P2_1$, where the inversion symmetry was lost, and the three molecules denoted as 1, 2, and 3 were independent of each other. This result suggests the structural phase transition at 80 K. The ethylene end groups at site 1 had a staggered conformation, whereas those

TABLE I. Crystallographic data at 300 K, 100 K, and 22 K.

T(K)	300 K	100 K	22 K
Space group	$P2_1/n$	$P2_1/n$	$P2_1$
a(Å)	9.4340(5)	9.3250(4)	9.3230(3)
b(Å)	30.646(1)	30.506(1)	30.3100(1)
c(Å)	8.5030(4)	8.3780(3)	8.3860(3)
β(deg)	98.661(4)	98.201(3)	98.100(3)
V(Å^3)	2430.3(2)	2358.9(2)	2346.1(1)
Z	2	2	2
No. of ref.[a]	4768	4609	5930
R	0.074	0.062	0.069
wR	0.220	0.198	0.204

[a] "No. of ref." denotes a number of independent reflections used for the structural analysis.

at site 2 and site 3 had eclipsed conformations. Therefore, the molecule 1 corresponds to I, and the molecules 2 and 3 correspond to the two equivalent molecules II. The same correspondence was obtained from the comparison of the relative positions between ET and $\mathrm{ReO_4^-}$.

It is well known that the geometry of ET has a close relationship with site charge.[17] When the site charge, ρ, of $\mathrm{ET}^{\rho+}$ increases from 0 to 1, the C$=$C bond lengths are lengthened and the C-S bond lengths are shortened. Guionneau *et al.* has given an empirical equation to relate bond lengths to ρ.[18] By using this relationship, we estimated ρ as $\sim+0.4$ for site I and $\sim+0.9$ for site II at 300 K, and $\sim+0.3$ for site I and $\sim+0.8$ for site II at 100 K. At 22 K, the site charges changed into $\sim+0.8$ at site 1, $\sim+1.2$ at site 2, and $\sim+0.4$ at site 3. As shown in Figs. 3(a) and 3(b), the bond-length analysis suggested that charge redistribution occurred at the phase transition. It should be noted that the estimated values have qualitative meaning, that is, ρ_{I} is smaller than ρ_{II}, and ρ_1 and ρ_2 are larger than ρ_3. In order to obtain a more quantitative estimation of ρ, we need the data of vibrational spectra, Which will be described in Sec. IV A.

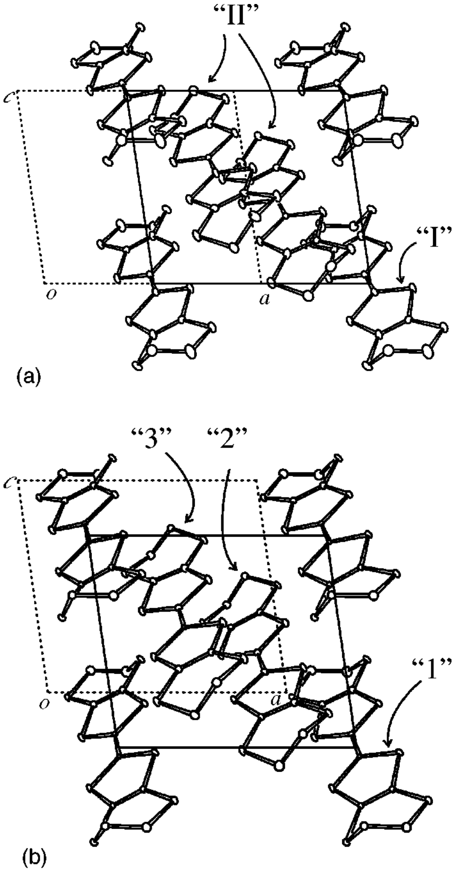

FIG. 3. Molecular arrangements in the conducting layers at (a) 100 K and (b) 22 K. Dotted lines show the crystallographic unit cells. The origins of the unit cells, drawn by solid lines, are shifted to the center of staggered molecules.

B. Spectral change in the phase transition

With decreasing temperature down to 80 K, no spectral change was observed except for the intensity enhancement and the linewidth narrowing of x1 and y1, as shown in Fig. 4(a). At 70 K, the additional peaks, X1, X3, Y1, Z2, and Z3, emerged, and x1 and y1 were replaced by these five peaks at 15 K. We consider that the drastic spectral change is associated with the structural phase transition. However, the spectral change began to occur at the temperature lower than 80 K. This difference in temperature comes from the elevation of the sample temperature due to the laser irradiation. The mixture of the high-temperature and low-temperature phases in the 60 K and 70 K spectra is probably ascribed to the inhomgeneous heating effect. The sample temperature is more reliable in the reflectivity experiment. Figure 4(b) shows the [102]-polarized $\sigma(\omega)$ spectra obtained after Kramers-Kronig transformation of the reflectance spectra measured on the (010) crystal face. The corresponding big spectral change was observed between 90 K and 80 K. Figure 4(c) shows the temperature dependence of the b-polarized reflectance spectra measured on the (201) face. This spectrum also changed discontinuously between 90 K and 80 K: z1 and z2 in the 90 K spectrum are replaced by Z1, Z2, and Z3 in the 80 K spectrum. More detailed temperature dependence near the phase transition temperature is displayed in the inset of Fig. 4(c). As shown in this figure, the spectrum changed discontinuously between 80 K and 81

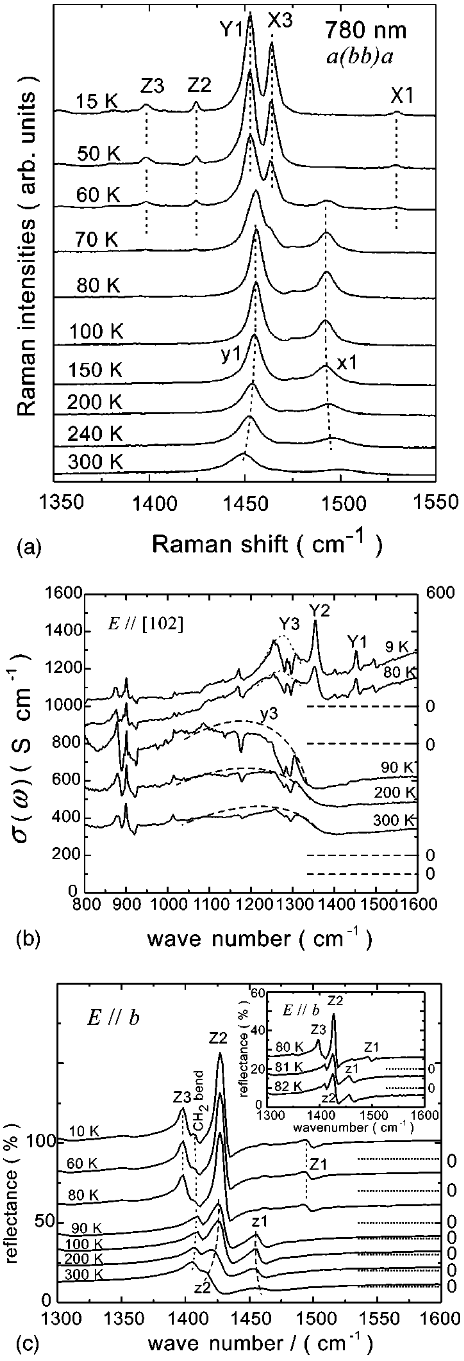

FIG. 4. (a) Temperature dependence of Raman spectra. The wavelength of excitation light is 780 nm. The experimental conditions are $a(bb)a$ configurations. (b) Temperature dependence of $\sigma(\omega)$ spectra obtained after Kramers-Kronig transformation of the [102]-polarized reflectance spectra. (c) Temperature dependence of b-polarized reflectance spectra. Data are accumulated for 500 scans. In the inset of (c), b-polarized reflectance spectra are shown, and a number scans for data collection is 128. The broken and dotted lines are guide for the eyes.

K. This observation also indicated the existence of the phase transition at 80 K. In the next section, we will discuss the nature of this phase transition.

IV. DISCUSSION

A. Interpretation of the phonon spectra

1. Factor group analysis (Ref. 19)

Table II shows the correlation diagram for Raman-active (a_g) and infrared-active (b_{lu}) modes. The unit cell contains two conducting layers, which are separated from each other by ReO_4^- layer. Since the interlayer interaction is much weaker than the interaction within the layer, the vibrational modes with A_g and B_g symmetry are expected to be degenerate, and those with A_u and B_u are also expected to be degenerate.[20] Therefore, the selection rule is effectively determined by the symmetry of the unit cell of a single layer. The number of observable band is at most two in the Raman spectrum and that is one in the infrared (IR) spectrum for an a_g mode. On the other hand, the number of observable band is at most two in the IR spectrum and that is one in the Raman spectrum for the b_{lu} mode. For the a_g mode, A_g and A_u at site II correspond to the in-phase and out-of-phase oscillation, respectively. The molecular phonons in the same conducting layer are interacting with each other through the *e-mv* interaction. Therefore, the a_g mode at site I mixes with the in-phase mode (A_g) at site II,[21] depending upon the magnitudes of the coupling constant of each a_g mode and the transfer integral between the site I and site II. The out-of-phase mode (A_u) at site II cannot mix with the a_g mode at site I.[21] Therefore, three vibronic modes with a_g symmetry are expressed by the following coordinates:

$$Q_{s1} = aQ_{\mathrm{I}} + \sqrt{1-a^2}(Q_{\mathrm{II}}^{\mathrm{A}} + Q_{\mathrm{II}}^{\mathrm{B}})/\sqrt{2}, \tag{1a}$$

$$Q_{s2} = \sqrt{1-a^2}Q_{\mathrm{I}} - a(Q_{\mathrm{II}}^{\mathrm{A}} + Q_{\mathrm{II}}^{\mathrm{B}})/\sqrt{2}, \tag{1b}$$

$$Q_r = (Q_{\mathrm{II}}^{\mathrm{A}} - Q_{\mathrm{II}}^{\mathrm{B}})/\sqrt{2}, \tag{1c}$$

where Q_{I}, $Q_{\mathrm{II}}^{\mathrm{A}}$, and $Q_{\mathrm{II}}^{\mathrm{B}}$ represent the normal coordinate at site I, that of the A molecule at site II, and that of the B molecule at site II, respectively. The symmetric coordinates Q_{s1} and Q_{s2} have A_g symmetry (Raman-active) and Q_r has A_u symmetry (IR-active). If the space group changes from $P2_1/n$ to $P2_1$ below the phase transition temperature, all of these modes mix with each other, and thereby the mutual exclusion rule between the Raman and IR spectra will be broken. We have measured the spectral region of the C=C stretching modes in the polarized infrared and polarized Raman spectra above and below the phase transition temperature, which are listed in Table II. The assignment of these bands will be discussed in the following two sections.

2. Phonon spectra above 81 K

Figure 5(a) shows the polarized Raman spectra measured at 100 K. Figure 5(b) shows the conductivity spectra after Kramers-Kronig transformation of the polarized reflectance spectra measured at 90 K. In this spectral region, the observable bands are C=C stretching modes (ν_2, 1460–1490 cm^{-1} and ν_3, <1460 cm^{-1}), CH$_2$ symmetric bending mode (ν_4, ~1400 cm^{-1}), CH$_2$ wagging mode (ν_5, 1280–1290 cm^{-1}), CH$_2$ twisting mode (~1180 cm^{-1}) in the

TABLE II. Correlation diagram for the ν_2, ν_3, and ν_{27} modes, and the observed frequencies.

T	Isolated molecule	Site		Unit cell	Unit cell of single layer	Selection rule	ν_2 (cm^{-1})	ν_3 (cm^{-1})	ν_{27} (cm^{-1})
$T > 81$ K	D_{2h}	C_i(I),	C_1(II)	C^5_{2h}	C_i				
	$6a_g(\nu_2, \nu_3)$	$2a_g$		A_g, B_g	A_g	Raman	x1 1492	y1 1455	
			$4a$	A_g, B_g	A_g	Raman	x2 1474	y2 1100–1400	
				A_u, B_u	A_u	IR		y3 900–1300	
	$6b_{1u}(\nu_{27})$	$2a_u$		A_u, B_u	A_u	IR			z1 1456
			$4a$	A_u, B_u	A_u	IR			z2 1423
				A_g, B_g	A_g	Raman			
$T < 80$ K	D_{2h}	$C_1(1,2,3)$		C^2_2	C_1				
							X1 1532	Y1 1453	
						Raman	X2 1475	Y2–1364	Z2 1425
							X3 1465	Y3–1300	Z3 1398
	$6a_g(\nu_2, \nu_3)$			$3A$	$3A$				
	$6b_{1u}(\nu_{27})$	$6a$		$3B$					
								Y1 1453	Z1 1495
						IR		Y2–1364	Z2 1423
								Y3–1300	Z3 1398

Raman spectrum, C═C stretching modes (ν_{27}, 1400–1460 cm^{-1}), CH$_2$ asymmetric bending mode (~1400 cm^{-1}), CH$_2$ wagging modes (1280–1290 cm^{-1}), and CH$_2$ twisting modes (1130–1180 cm^{-1}) in the IR spectrum.[22,23] $y1$ was observed very strongly in the $a(bb)a$ polarization. This polarization dependence is characteristic of the ν_3 modes.[24] Therefore, $y1$ was assigned to one of the A_g modes of ν_3, and therefore $x1$ and $x2$ were assigned to the A_g modes of ν_2 (see Table II). Since the *e-mv* coupling constant of ν_2 is significantly small,[22] the mixing between site I and site II is expected to be small. Therefore, the A_g modes for ν_2 are expressed by Eqs. (1a) and (1b) with $a \sim 1$. Then, Q_{s1} and Q_{s2} approximately correspond to the a_g mode at site I and the in-phase mode at site II, respectively. By comparing the result of the bond-length analysis, x1 and x2 were straightforwardly assigned to the ν_2 modes of site I and site II, respectively. The ν_2 mode has a liner relationship approximately against ρ.[25] Therefore, the site charges, ρ_{I} and ρ_{II}, were estimated from the peak separation between x1 and x2. By use of the frequency shift, $\Delta\nu_2 = 90$ cm$^{-1}/e$,[5] ρ_{I} and ρ_{II} were estimated to be $\sim +0.5_3$ and $\sim +0.7_3$, respectively.

Here we discuss the three peaks at 1400–1460 cm^{-1} in the b-polarized $\sigma(\omega)$ spectrum [Fig. 5(b)]. First of all, vibronic bands cannot appear in the b-polarized $\sigma(\omega)$ spectrum, because the b axis is perpendicular to the conducting plane. Since the long axis of ET is nearly parallel to the b axis, the IR-active b_{1u} mode, which is free from the *e-mv* interaction, is observable in the b-polarized $\sigma(\omega)$ spectrum. In this spectral region, ν_{27} (b_{1u}) (see Fig. 1) and CH$_2$ bending mode are observable. It is known that the ν_{27} mode shows a significant frequency shift depending upon the charge on ET, whereas the CH$_2$ bending mode is independent of the site charge.[22] As shown in Fig. 4(c), z1 and z2 exhibited characteristic temperature dependence around the phase transition temperature. Since the x-ray experiment suggested that the charge distribution was significantly reorganized below the phase transition temperature, we assigned z1 and z2 to the A_u modes of ν_{27} at site I and site II, respectively.[26] The remaining 1410 cm^{-1} band was located close to the asymmetric CH$_2$ bending mode.[22] Therefore, the 1410 cm^{-1} band was assigned to this mode.[27] The frequency of this band was actually independent of the phase transition [see Fig. 4(c)]. By use of the frequency shift, $\Delta\nu_{27} = \sim 105$ cm$^{-1}/e^{+}$, from our experiments,[26] ρ_{I} and ρ_{II} were estimated to be $\sim +0.4_6$ and $\sim +0.7_7$, respectively. These values are in agreement with those estimated from ν_2 within the accuracy of ~0.1.

Since the *e-mv* coupling constant of ν_3 is much larger than that of ν_2, the ν_3 mode is expected to show a large splitting. If the *e-mv* interaction overcome the site-energy difference between the site I and site II, the A_g modes for ν_3 is expressed by Eqs. (1a) and (1b) with $a \approx 1/\sqrt{3}$. As we have discussed above, y1 was assigned to one of the A_g mode of ν_3. The Q_{s1} mode in Eq. (1a) corresponds to the in-phase oscillation at every site, when $a \approx 1/\sqrt{3}$. So this mode hardly induces the charge-transfer among the sites I, II$_{\mathrm{A}}$, and II$_{\mathrm{B}}$. Therefore, the frequency of Q_{s1} is highest among Q_{s1}, Q_{s2}, and Q_r, and the linewidth of Q_{s1} is not broadened unlike other two modes. Therefore, we assigned the y1 band with a narrow bandwidth to the Q_{s1} mode. Another A_g mode, Q_{s2}, is perturbed by the *e-mv* interaction, since the oscillations at sites I and II have an out-of-phase relation.[28] The frequency of Q_{s2} is downshifted and the linewidth becomes very broad through the *e-mv* effect. The y2 band, which we managed to find very weakly in the $b(cc)b$- and $b(aa)b$-polarized spectra in the inset of Fig. 5(a), may be the candidate of the Q_{s2} mode. The very broad linewidth over 200 cm^{-1} of y2 assisted this assignment. Several anti-resonance modes are

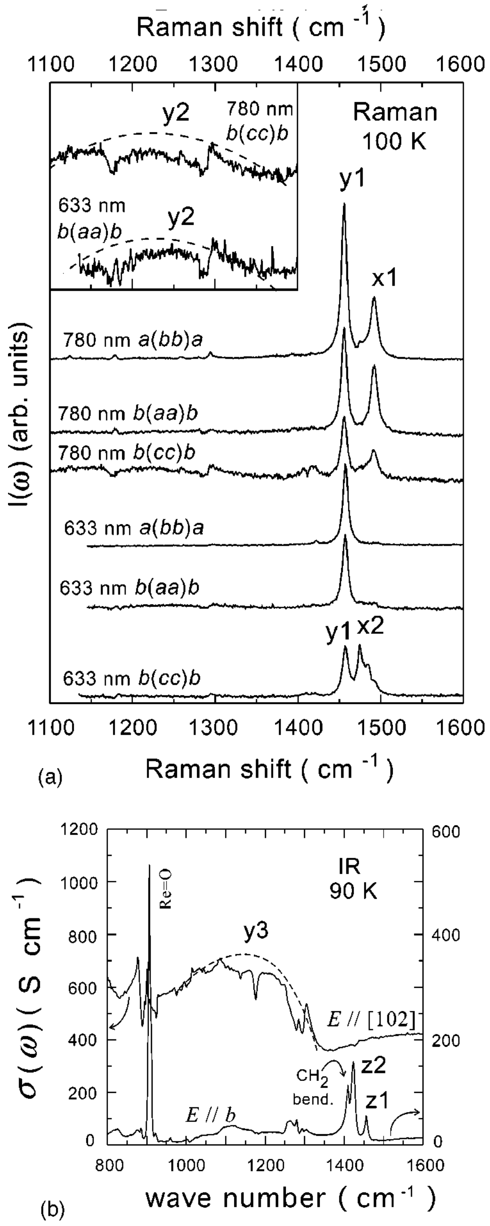

FIG. 5. (a) Polarized Raman spectra measured at 100 K. The wavelength of the excitation light is 780 nm and 633 nm. The experimental configurations are $a(bb)a, b(aa)b$, and $b(cc)b$. The inset shows the spectra enlarged along ordinate. (b) $\sigma(\omega)$ spectra obtained after Kramers-Kronig transformations of [102]-polarized (top) and b-polarized (bottom) reflectance spectra at 90 K. Broken line is a guide for the eyes.

superimposed on this band. These modes were assigned to the CH_2 wagging mode and the CH_2 twisting mode.[22,23] The A_u mode, Q_r, for ν_3 is infrared active and usually has a strong intensity and broad linewidth through the *e-mv* interaction between A and B molecules at site II.[28] Indeed, the broad band, y3, with several antiresonance modes in [102]-polarized $\sigma(\omega)$ spectrum [Fig. 5(b)] is characteristic of the vibronic mode. Therefore, the y3 band was assigned to the A_u mode, Q_r of ν_3. The above explanation for the frequency shift of the ν_3 vibronic modes was qualitatively confirmed using the symmetric trimer model shown in Appendix. We were able to assign x, y, and z bands successfully using the results of the factor group analysis. This implies that the existence of the inversion center, which certifies $P2_1/n$, is spectroscopically confirmed.

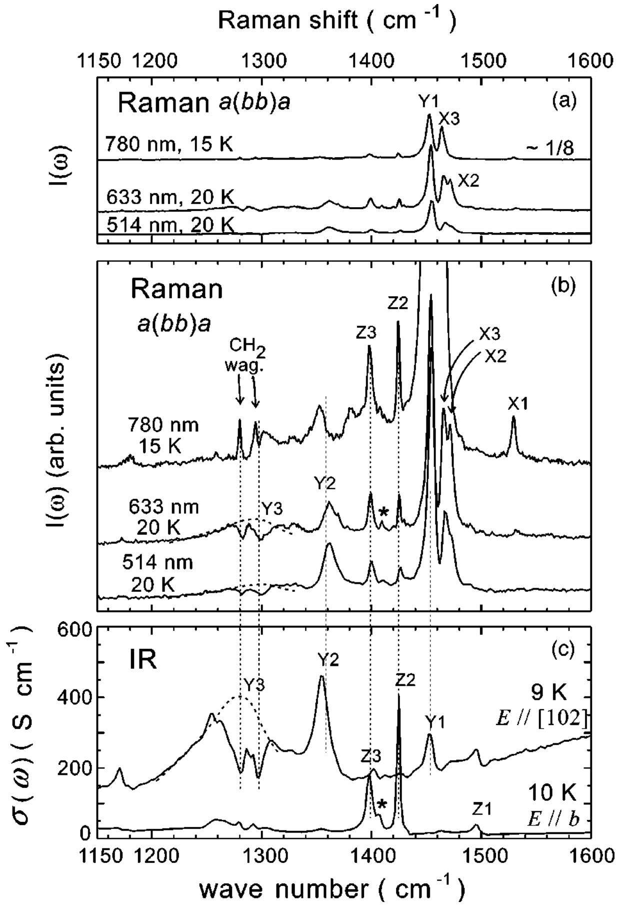

FIG. 6. (a) Polarized Raman spectra measured at the lowest temperature in each measurement. The wavelength of the excitation light is 780 nm (top), 633 nm (middle) and 514 nm (bottom). The experimental configuration is $a(bb)a$. (b) The same spectra as shown in (a). The spectra are enlarged along ordinate in order to show the weak bands. The spectral data, obtained with a 780 nm laser, are omitted from 1442 cm^{-1} to 1470 cm^{-1}. (c) $\sigma(\omega)$ spectra obtained after Kramers-Kronig transformations of [102]-polarized (top) and b-polarized (bottom) reflectance spectra at the lowest temperature in each measurement. The asterisks denote CH_2 bending modes. The broken and dotted lines are guides for the eyes.

3. Phonon spectra below 80 K

Figures 6(a) and 6(b) display the Raman spectra at the lowest temperatures with the $a(bb)a$ geometry. Almost the same spectral features were observed with different relative intensities in the $b(aa)b, b(ac^*)b, b(cc)b, c(a^*b)c$, and $a(bc^*)a$ geometries. The isolated band, X1, was safely assigned to ν_2, because ν_2 is located above $\sim$1460 cm^{-1} for ρ=1, and because ν_3 is located below 1490 cm^{-1} for ρ=0.[22] The frequency of X1 is close to that of ν_2 of ET^0($\sim$1550 cm^{-1}).[22] The bands, X2, X3, and Y1, were closely located at the boundary between ν_2 and ν_3. Y1 was observed most strongly in the $a(bb)a$ spectrum. This polar-

TABLE III. Transfer integrals at 300 K, 100 K, and 22 K. The directions are defined in the 22 K unit cell shown in Fig. 3(b). Subscripts of r,p, and q denote the adjacent ET molecules.

		300 K	100 K			22 K	
		t_{ij} (meV)	t_{ij} (meV)	Symbol[a]		t_{ij} (meV)	Symbol[a]
	$r_{\text{I-II}}$	−76.8	−86.7	···	r_{12}	−66.0	···
$[\bar{1}01]$					r_{31}	−91.3	···
	$r_{\text{II-II}}$	66.7	67.3	···	r_{23}	79.3	···
	$p_{\text{I-II}}$	115.1	127.7	···	p_{12}	153.5	—
[201]					p_{31}	−134.6	—
	$p_{\text{II-II}}$	133.5	153.4	—	P_{23}	116.1	---
	$q_{\text{I-II}}$	271.3	286.3	═	q_{12}	157.8	—
[102]					q_{31}	296.8	═
	$q_{\text{II-II}}$	−149.2	−160.8	—	q_{23}	−306.0	═

[a] Symbols show the magnitudes of transfer integrals, and they are used in Fig. 7 to show the distribution of transfer integrals.

ization dependence is characteristic of the ν_3 mode as described in the preceding section. Therefore X2 and X3 were likely to be assigned to ν_2. This assignment was consistent with the bond-length analysis that suggested the existence of the crystallographically independent three molecules. By comparing the result of the bond-length analysis, X1, X2, and X3 were assigned to ν_2 at site 3, site 1, and site 2, respectively. Three bands, Z1, Z2, and Z3 in the b-polarized $\sigma(\omega)$ spectrum [see Fig. 6(c)] were assigned to ν_{27} from the same reason for the assignment of z1 and z2 described in the preceding paragraph. In addition, Z1 and Z3 were observed only below the phase transition temperature. Therefore, Z1, Z2, and Z3 were assigned to ν_{27} at site 3, site 1, and site 2, respectively. The site charge, ρ, was estimated from peak positions among X1–X3 as $\rho_3=+0.2$, $\rho_1=+0.8_5$, and $\rho_2=+0.9_5$, using the relation, $\Delta\nu_2=90\ \text{cm}^{-1}/e$.[5] By use of the frequency shift, $\Delta\nu_{27}=\sim 105\ \text{cm}^{-1}/e^{+}$,[26] ρ was estimated from peak positions among Z1–Z3 as $\rho_3=\sim+0.1_5$, $\rho_1=\sim+0.8_0$, and $\rho_2=\sim+1.0_4$, respectively. These values are in agreement with those estimated from ν_2 within the accuracy of ~0.1.

Y2 and Y3 in Figs. 6(b) and 6(c) had a broad linewidth. In addition, Y2 and Y3 in the $\sigma(\omega)$ spectrum were polarized in the conducting plane with a strong intensity. A strong intensity, broad linewidth, polarization direction, and large downshift from the unperturbed frequency are characteristic of a vibronic mode with a large *e-mv* coupling constant.[28] Therefore, Y1, Y2, and Y3 were assigned to the three vibronic modes of ν_3. Since the charge at site 1 is approximately identical to the charge of site 2, we analyzed further assignment using a symmetric trimer model shown in the Appendix. When $\rho_c=0.2$ [see Fig. 8(a) in the Appendix], Q_{s1} is the ν_3 vibronic mode nearly localized at site 3, and Q_{s2} and Q_r are localized rather at site 1 and site 2. As shown in Fig. 8(b), the frequency of Q_{s1} is insensitive to the site charge in the region of $0.3<\rho_c<1$, whereas those of Q_{s2} and Q_r are very sensitive in the whole region. The position of Y1 was close to y1, while Y2 and Y3 were observed at the frequencies significantly higher than those of y2 and y3 (see Table II). Therefore, we assigned Y1 to Q_{s1}, Y2 to Q_{s2}, and Y3 to Q_r, comparing the frequencies of these bands to the model calculation. The integrated intensity of Y3 is larger than that of Y2. This is consistent with the above assignment, because Q_{s2} is infrared inactive if the site 1 and site 2 is exactly symmetric. Because the site 1 is not exactly equivalent to the site 2, Q_{s1}, Q_{s2}, and Q_r are mixed with each other. Indeed, Y1–Y3 were observed in both the Raman and IR spectra at the same positions and with the same line shapes, that is, a mutual exclusion rule was broken (see Table II). This result is strong evidence for the breaking of the center of symmetry at 80 K.

B. Characterization of the metal-insulator phase transition

We consider that the structural phase transition accompanied by a drastic spectral change is responsible for the metal-insulator transition.[12,13] Let us examine the molecular arrangement above and below the phase transition temperature. As shown in Fig. 2, the b axis was shortened discontinuously at 80 K. The contraction of the b axis suggested a tilting of the ET molecules against the conducting layer. We calculated the inclination angle, δ, defined as the angle between the long molecular axis of ET and the (010) plane. The inclination angles decreased from $\delta_{\text{I}}=58.1°$ and $\delta_{\text{II}}=58.2°$ at 100 K to $\delta_1=55.5°$, $\delta_2=57.3°$, and $\delta_3=57.4°$ at 22 K.[29] This structural change will be reflected on the distribution of transfer integrals, t_{ij}. Based on the crystal structures determined at 300, 100, and 22 K, we calculated t_{ij} assuming the empirical relation, $t_{ij}=-10S_{ij}$, where S_{ij} is an overlap integral of HOMO (highest occupied molecular orbital) of ET at site i and site j.[30] The transfer integrals thus obtained are listed in Table III. Various lines shown in Table III denote the qualitative magnitude of transfer integrals. Using these symbols, the distribution of the transfer integrals are schematically drawn in Fig. 7 along with the site-charge distribution. Between 300 K and 100 K, each $|t_{ij}|$ increased at low temperature without changing their ratios. This change corresponds to the monotonous thermal contraction in the metallic phase. At 22 K, however, the distribution of t_{ij} changed as shown in Fig. 7(b). Using these transfer integrals, we calculated the tight-binding band at 100 K and 22 K in order to examine whether this structural change extinguishes the electron and

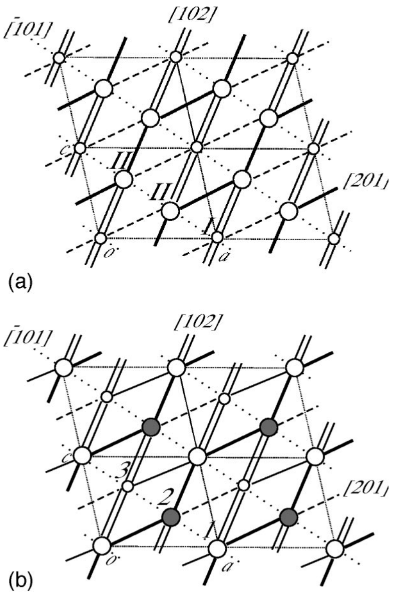

FIG. 7. The schematic drawing to show the distribution of ρ and transfer integrals (a) at 100 K and (b) at 22 K. The origins of the unit cells are shifted to the center of staggered ET. (a) The large open circle denotes the charge-rich ($\rho_{\mathrm{II}}=0.7_3$) site, and the small open circle denotes the charge-poor ($\rho_{\mathrm{I}}=0.5_3$) site. (b) The large solid and open circles denote the charge-rich sites ($\rho_2=0.9_5$ and $\rho_1=0.8_5$), and the small open circle denotes the charge-poor ($\rho_3=0.2$) site. ET molecules are bonded to each other by the symbols that show the qualitative magnitude of transfer integrals (see Table III).

hole pockets in the semimetallic band. However, the electron pocket centered at the Z point and the hole pocket centered at the Γ point showed no significant change at 22 K. Therefore, a simple band picture cannot explain the metal-insulator transition.

As discussed in Sec. IV A, a big difference was found in the site-charge distribution between the metallic and insulating phases. Below the phase transition temperature, the holes were almost completely localized at site 1 and site 2, whereas the charge distribution was much more homogeneous above the phase transition temperature. Consequently, we consider that the low-temperature phase is a CO state, and this CO state is responsible for the insulating behavior in resistivity. This is the first experiment that verified the CO state in the β''-type ET salts. As shown in Fig. 7(b), the charge-rich sites bonded by p_{12} and q_{12} are arranged along the [101] direction, forming a zigzag stripe. These charge stripes are weakly connected by r_{12}, and therefore the charge-rich sites form a honeycomb network.

Let us review the past experiments from the viewpoint of the CO state that has the distribution of the charges and bonds (transfer integrals) shown in Fig. 7(b). Yakushi *et al.* reported a new hump at 6500 cm^{-1} in the [102]-polarized $\sigma(\omega)$ spectrum below the phase transition temperature.[13] They ascribed this hump to the interband transition in the folded 2/3-filled band or charge-transfer transition between ET^{+}. The CO state can generate a locally excited state involving U such as $\mathrm{M}(1)^{+}\mathrm{M}(2)^{+}\rightarrow\mathrm{M}(1)^{0}\mathrm{M}(2)^{2+}$, where M($i$) denotes the molecule at site i. This type of optical transition is polarized along the [102] and [201], because the charge-rich sites are connected by intermediate magnitude of transfer integrals, q_{12} and p_{12}, [see the pair of open and solid circles in Fig. 7(b)]. Therefore, the latter interpretation is appropriate for understanding the new hump. Incidentally, the corresponding optical transition has been reported in other compounds such as α-$(\mathrm{ET})_2\mathrm{I}_3$ (Ref. 7) and $\mathrm{Cs}_2(\mathrm{TCNQ})_3$ (Ref. 31). Generally, the localized hole has spin degrees of freedom. Carneiro *et al.* reported the ESR experiment for the single crystal of this compound.[11] With decreasing temperature, the relative ESR intensity gradually decreased down to about 88 K, and changed the slope to an activation type with the activation energy of 90 K below 88 K. This magnetic behavior is very different from those of θ-$(\mathrm{ET})_2\mathrm{RbZn(SCN)}_4$,[32] θ-$(\mathrm{BDT\text{-}TTP})_2\mathrm{Cu(NCS)}_2$,[33] and $(\mathrm{TMTTF})_2\mathrm{AsF}_6$[34] in which the magnetic transition occurred at much lower temperature than T_{CO}. In β''-$(\mathrm{ET})_3(\mathrm{ReO}_4)_2$, the magnetic transition occurred at approximately the same temperature of the CO transition. In the CO state of θ-type ET salts and $(\mathrm{TMTTF})_2\mathrm{AsF}_6$, the localized charges are arranged effectively one dimensionally with a uniform transfer integral (no spin gap). On the other hand, in β''-$(\mathrm{ET})_3(\mathrm{ReO}_4)_2$, the charge-poor site 3 is bonded to the charge-rich sites 1 and 2 through the largest transfer integrals (double line), q_{23} and q_{31}, forming a trimer unit $(1=3=2)$. Possibly, this trimer unit contributes to form a spin singlet. Below T_{CO}, the ESR signal split into two, which have different angular dependences.[11] Carneiro *et al.* interpreted that the split signals were attributed to the species in different layers separated by ReO_4^- in the unit cell, and that these two species were decoupled below the phase transition temperature. This interpretation was later supported by other experiments, in which the ESR signal did not show such a g-splitting for β''-$(\mathrm{ET})_3(\mathrm{HSO}_4)_2$ and β''-$(\mathrm{ET})_3(\mathrm{ClO}_4)_2$, which consist of a single organic layer.[35,36] The reason for the decoupling below T_{CO} can be explained by the localization of the charge within the layer, which will also suppress the interlayer hopping. Although the behavior of the electrical resistivity is slightly different between Refs. 12 and 13, the resistivity has a minimum at $T_m\approx 150$ K. The temperature, T_m, is significantly higher than $T_{\mathrm{CO}}\approx 80$ K. The difference between T_m and T_{CO} is commonly found in θ-$(\mathrm{ET})_2\mathrm{RbZn(SCN)}$, ($T_m>300$ K, $T_{\mathrm{CO}}=180$ K),[32] θ-$(\mathrm{BDT\text{-}TTP})_2\mathrm{Cu(NCS)}_2$ ($T_m>300$ K, $T_{\mathrm{CO}}=250$ K),[33] and $(\mathrm{TMTTF})_2\mathrm{AsF}_6$ ($T_m=230$ K and $T_{\mathrm{CO}}=100$ K).[37,38] It should be noted that the charge has a nearly localized nature before the CO phase transition in all of these compounds.

V. CONCLUSION

In conclusion, the metal-insulator phase transition of β''-$(\mathrm{ET})_3(\mathrm{ReO}_4)_2$ was characterized as a charge-ordering phase transition accompanied by a structural change with the loss of a center of symmetry. The charge distribution changed from a nearly homogeneous delocalized state to a strongly localized state. The localized holes are arranged along the [101] direction, forming a zigzag stripe. A structural change accompanying the CO phase transition brought about the redistribution in the transfer integral network. The strongest transfer integrals form a trimer unit, in which a charge-poor site is sandwiched by two charge-rich sites. The vibronic bands in the IR and Raman spectra were qualitatively interpreted based on the symmetric trimer model.

ACKNOWLEDGMENTS

This research was partly supported by a Grant-in-Aid for Scientific Research (No. 13440214) and a Grant-in-Aid for Scientific Research on Priority Areas of Molecular Conductors (No. 15073223) from the Ministry of Education, Culture, Sports, Science and Technology of Japan.

APPENDIX: CALCUATION OF THE FREQUENCY SHIFT OF VIBRONIC MODES USING A SYMMETRIC TRIMER MODEL

In order to examine how each vibronic ν_3 mode shows a downshift caused by an *e-mv* effect, we conducted a model calculation of the frequency shifts for the modes, Q_{s1}, Q_{s2}, and Q_r, in Eqs. (1a)–(1c). The ET molecules in β''-(ET)$_3$(ReO$_4$)$_2$ consists of a trimer unit as shown in Fig. 7(a) (II=I=II) and Fig. 7(b) (1=3=2). We applied the Yartsev's symmetric linear trimer model[39] to this trimer unit. The Hamiltonian is expressed as follows ($\hbar=1$),

$$H = H_e + H_v + H_{ev}, \tag{A1}$$

$$H_e = \sum_{i}^{3} D_i n_i + \sum_{\sigma} \sum_{i\neq j}^{3} t_{ij}(c_{i\sigma}^{+}c_{j\sigma} + c_{j\sigma}^{+}c_{i\sigma}) + U\sum_{i=1}^{3} n_{i\uparrow}n_{i\downarrow} + \sum_{i\neq j}^{3} V_{ij}n_i n_j, \tag{A2}$$

$$H_v = \frac{1}{2}\sum_{i}^{3}(P_i^2 + Q_i^2\omega_i^2), \tag{A3}$$

$$H_{ev} = g\sum_{i}^{3} n_i\sqrt{2\omega_i}Q_i, \tag{A4}$$

where i and j denote the site numbers, t_{ij} is the transfer integral between the sites i and j, $c_i^+(c_i)$ is the creation (annihilation) operator with the σ spin, $n_i = c_i^+ c_i$ is the number operator, and D_i is the site energy at site i. The on-site Coulomb energy, U, and the intersite Coulomb interaction, V, were fixed to 0.8 eV and 0.2 eV, respectively.[40] P_i and Q_i, respectively, denote the momentum operator and the normal coordinate at ith site. The *e-mv* coupling constant, g, of ν_3 was assumed to be 0.1 eV.[22] ω_i was the unperturbed frequency of ith site, in which the linear relation was assumed to be $\omega_i = 1416 + 74(1-\rho_i)$ cm^{-1}, where ρ_i was the charge at ith site.[22] The Q dependence of the ground state energy was calculated using the perturbation method,[41] in which Q consists of Q_{s1}, Q_{s2}, and Q_r,

$$E(Q) = E_1 + \langle\Psi_1|H_{ev}(Q)|\Psi_1\rangle + \sum_{m=2}^{9}\frac{|\langle\Psi_1|H_{ev}(Q)|\Psi_1\rangle|^2}{E_1 - E_m}, \tag{A5}$$

where E_m denotes the energy of the electronic excited states, and Ψ_m is the corresponding wave function. Nine singlet electronic states are incorporated into the calculation. The perturbed frequencies of the symmetric mode, Q_{s1} and Q_{s2} were obtained by constructing the force constant matrix composed of the second derivative of $E(Q)$ by Q_{s1} and Q_{s2}.[41] The coefficient, a, was obtained after normalizing the eigenvectors of the force constants matrix. The frequency of the asymmetric mode, Q_r, was obtained from the second derivative of $E(Q)$ by Q_r. The site charge, ρ_i, calculated using the following equation:

$$\rho_i = \langle\Psi_1|n_i|\Psi_1\rangle \tag{A6}$$

was varied by changing the site energy, D_i.

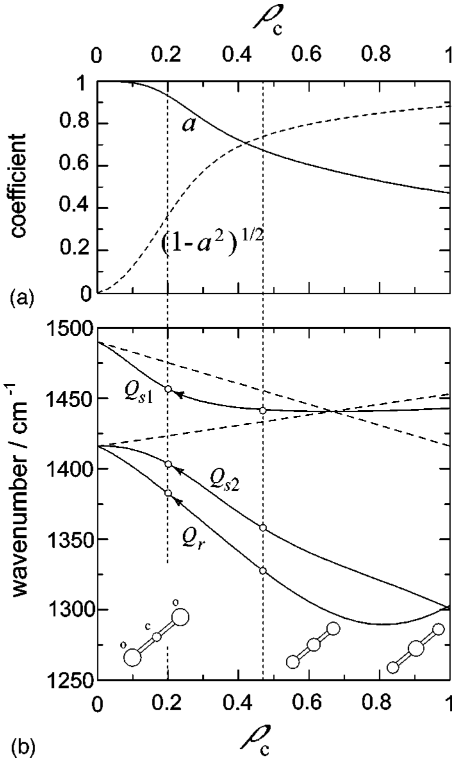

FIG. 8. (a) Site-charge (ρ_c at the central site) dependences of the coefficients, a (solid line) and $(1-a^2)^{1/2}$ (broken line), defined in Eqs. (1a) and (1b) in the text. (b) ρ_c dependences of the frequencies of ν_3 perturbed by the *e-mv* interaction. Broken lines show the unperturbed frequencies of ν_3 modes. Schematic views of the symmetric trimers are shown in the bottom of the figure. The areas of the opened circles correspond to the site-charges.

Figure 8(a) shows ρ_c (the charge at the central site) dependence of the coefficient, a and $(1-a^2)^{1/2}$, given in Eqs. (1a) and (1b). Figure 8(b) shows the ρ_c dependence of the perturbed frequency of each mode. When $\rho_c=0$, the charges are completely localized at the outer sites. In this case, Q_{s2}

and Q_r are degenerate modes and located at outer sites ($\rho_o = 1$), and Q_{s1} mode is located at central site ($\rho_c = 0$). With increasing ρ_c, the A_g modes at the central and outer sites mix with each other, and the frequency of each mode shows a downshift. At the same time the degenerate modes, Q_{s2} and Q_r, are split. When $\rho_c < \sim 0.4$, the central (outer) molecule mostly contributes to Q_{s1} (Q_{s2}), while the outer (central) molecule mostly contributes to Q_{s1} (Q_{s2}) in the range of $\rho_c > \sim 0.4$. Q_r consists of the vibrations of outer molecules in a whole range of ρ_c because of the symmetry. Very interestingly, the frequency Q_{s1} quickly approaches the frequency of the average charge of $\rho = 2/3$ and becomes independent of ρ_c in the range of $\rho_c > \sim 0.3$, whereas the frequencies of Q_{s2} and Q_r very depend on ρ_c.

---

*Electronic address: yamataka@ims.ac.jp

[1] For example see, “Highly conducting quasi one-dimensional organic crystals, ” in *Semiconductors and Semimetals*, edited by E. Conwell (Academic, London, 1988), Vol. 27; A. Graja, *Low Dimensional Organic Conductors* (World Scientific, Singapore, 1992).

[2] K. Kanoda, Kotai Butzuri (in Japanese) **30**, 84 (1994).

[3] K. Kanoda, Hyperfine Interact. **104**, 235 (1997).

[4] K. Miyagawa, A. Kawamoto, and K. Kanoda, Phys. Rev. B **62**, R7679 (2000).

[5] K. Yamamoto, K. Yakushi, K. Miyagawa, K. Kanoda, and A. Kawamoto, Phys. Rev. B **65**, 085110 (2002).

[6] M. Watanabe, Y. Noda, Y. Nogami, H. Mori, and S. Tanaka, Synth. Met. **133–134**, 283 (2003).

[7] R. Wojciechowski, K. Yamamoto, K. Yakushi, and A. Kawamoto, Phys. Rev. B **67**, 224105 (2003).

[8] J. Merino and R. H. McKenzie, Phys. Rev. Lett. **87**, 237002 (2001).

[9] Structural data for β''-salts are summarized in, T. Mori, Bull. Chem. Soc. Jpn. **71**, 2509 (1998).

[10] This salt was first named α-(ET)$_3$(ReO$_4$)$_2$. Based on the classification by Ref. 9, this salt is classified into β''_{321}-structure. In the followings, we denote α-(ET)$_3$(ReO$_4$)$_2$ as β''-(ET)$_3$(ReO$_4$)$_2$.

[11] K. Carneiro, J. C. Scott, and E. M. Engler, Solid State Commun. **50**, 477 (1984).

[12] S. S.P. Parkin, E. M. Engler, V. Y. Lee, and R. R. Schumaker, Mol. Cryst. Liq. Cryst. **119**, 375 (1985). In the literature, the dR/dT changed the sign at ~150 K, and the resistivity steeply increased at ~100 K They defined the metal-insulator transition temperature as 100 K.

[13] K. Yakushi, H. Kanbara, H. Tajima, H. Kuroda, G. Saito, and T. Mori, Bull. Chem. Soc. Jpn. **60**, 4251 (1987). The temperature of the resistivity minimum, ~150 K, in Ref. 12 is in agreement with that in Ref. 13. However, the resistivity steeply increased at ~85 K in Ref. 13.

[14] S. M. Baker, J. Dong, G. Li, Z. Zhu, J. L. Musfeldt, J. A. Schlueter, M. E. Kelly, R. G. Daugherty, and J. M. Williams, Phys. Rev. B **60**, 931 (1999).

[15] G. M. Sheldrick, SHELEXL97, University of Göttingen, Göttingen, Germany, 1997.

[16] H. Kanbara, H. Tajima, S. Aratani, K. Yakushi, H. Kuroda, G. Saito, A. Kawamoto, and J. Tanaka, Chem. Lett. **1986**, 437 (1986).

[17] H. Kobayashi, A. Kobayashi, Y. Sasaki, G. Saito, and H. Inokuchi, Chem. Lett. **1984**, 183 (1984).

[18] P. Guionneau, C. J. Kepert, D. Chasseau, M. R. Truter, and P. Day, Synth. Met. **86**, 1973 (1997).

[19] The symmetry of molecular and crystal phonons is represented by lowercase and uppercase letters.

[20] The B_g mode should be observed in the Raman spectrum with the polarization of $a(bc^*)a$ and $c(a^*b)c$. However, we were not able to observe the corresponding mode, because of its weak intensity.

[21] The in-phase (A_g) mode at site II is consists of the a_g modes at sites II$_\mathrm{A}$ and II$_\mathrm{B}$. The out-of-phase mode (A_u) at site II is consists of the a_g modes at sites II$_\mathrm{A}$ and II$_\mathrm{B}$

[22] M. E. Kozlov, K. I. Pokhodnia, and A. A. Yurchenko, Spectrochim. Acta, Part A **43**, 323 (1987); **45**, 437 (1989); J. E. Eldridge, C. C. Homes, J. M. Williams, A. M. Kini, and H. H. Wang, *ibid.* **51**, 947 (1995).

[23] E. Demiralp, S. Dasgupta, and W. A. Goddard III, J. Phys. Chem. **101**, 1975 (1997).

[24] M. Maksimuk, K. Yakushi, H. Taniguchi, K. Kanoda, and A. Kawamoto, J. Phys. Soc. Jpn. **70**, 3728 (2001).

[25] H. H. Wang, J. R. Ferraro, J. M. Williams, U. Geiser, and J. A. Schlueter, J. Chem. Soc., Chem. Commun. **1994**, 1893 (1994). In this reference, ν_2 is designated as ν_3.

[26] According to Ref. 22, the infrared modes at 1505 cm^{-1} and 1445 cm^{-1} were assigned to ν_{27} of ET^0 and ET$^+$, respectively. If we apply the relation, $\Delta\nu_{27} = 60$ cm$^{-1}/e^+$ in Ref. 22, to Z2 and Z3, the site-charge difference is estimated to be $\rho_2 - \rho_3 = 1.6$, which is unacceptable for ET. We believe that the assignment of ν_{27} of ET$^+$ in Ref. 22 is possibly ambiguous, because the distinction from vibronic ν_2 is not straightforward in the powder spectrum. We measured the polarized reflectance and Raman spectrum of ET$^+$(AuCl$_2$Br$_2$)$^-$ [T. Yamamoto, M. Uruichi, A. Ugawa, and K. Yakushi (unpublished)] , in which the crystallographic b-direction almost exactly corresponds to the long axis of ET, and ν_{27} is expected to be polarized along this direction. Indeed, the strongest peak was observed at ~1400 cm^{-1} along with the CH$_2$ bending modes in the b-polarized reflectance spectrum. On the other hand, ν_2 was observed at ~1447 cm^{-1} in the Raman spectrum. Therefore, the ~1400 cm^{-1} band was assigned to ν_{27} of ET$^+$ and the frequency shift of ν_{27} is estimated to be $\Delta\nu_{27} = \sim 105$ cm$^{-1}/e^+$.

[27] Our assignment for the ν_{27} and CH$_2$ bending mode were supported also from the comparison between the infrared spectrum of the quarter-filled salts, β''-(ET)$_4$Pt(CN)$_4$H$_2$O, and that of deuterium-substituted analogue, β''-(d$_8$-ET)$_4$Pt(CN)$_4$H$_2$O [T. Yamamoto, M. Uruichi, K. Yakushi, and A. Kawamoto (unpublished)] . Since the 1410 cm^{-1} band in the former salt moved to 1130 cm^{-1} in the latter salt, this band was assigned to the CH$_2$ (or CD$_2$) bending mode. On the other hand, the strongest doublet centered at ~1450 cm^{-1} showed no peak shift. Thus, this doublet was assigned to ν_{27}. This behavior is in agreement with that ν_2 was observed as the doublet centered at ~1490 cm^{-1}.

[28] A. Painelli, C. Pecile, and A. Girlando, Mol. Cryst. Liq. Cryst.

134, 1 (1986); V. M. Yartsev and R. Sweitlik, Rev. Solid State Sci. **4**, 69 (1990).

[29] The contraction of the b axis, Δb, agreed well with the calculated value using the equation, $\Delta b = 2m/3(\sin\delta_{\mathrm{I}} + 2\sin\delta_{\mathrm{II}}) - 2m/3(\sin\delta_1 + \sin\delta_2 + \sin\delta_3)$, where m denotes the length of ET molecule (~13 Å).

[30] T. Mori, A. Kobayashi, Y. Sasaki, H. Kobayashi, G. Saito, and H. Inokuchi, Bull. Chem. Soc. Jpn. **57**, 627 (1984).

[31] K. Yakushi, M. Iguchi, G. Katagiri, T. Kusaka, T. Ohta, and H. Kuroda, Bull. Chem. Soc. Jpn. **54**, 348 (1981).

[32] H. Mori, S. Tanaka, and T. Mori, Phys. Rev. B **57**, 12 023 (1998).

[33] K. Yakushi, K. Yamamoto, M. Simonyan, J. Ouyang, and C. Nakano, Phys. Rev. B **66**, 235102 (2002).

[34] D. Jerome, P. Auban-Senzier, L. Balicas, K. Behnia, W. Kang, P. Wzietek, C. Perthier, and P. Caretta, Synth. Met. **70**, 719 (1995).

[35] A. Miyazaki, T. Enoki, H. Uekusa, and Y. Ohashi, Phys. Rev. B **55**, 6847 (1997).

[36] T. Enoki, K. Tujikawa, K. Suzuki, A. Uchida, and Y. Ohashi, Phys. Rev. B **50**, 16 287 (1994).

[37] T. Ishiguro and K. Yamaji, *Organic Superconductors*, Solid State Sciences 88 (Springer-Verlag, Berlin, Heidelberg, New York, London, Paris, Tokyo, Hong Kong, 1990).

[38] D. S. Chow, F. Zamborszky, B. Alavi, D. J. Tantillo, A. Baur, C. A. Merlic, and S. E. Brown, Phys. Rev. Lett. **85**, 1698 (2000).

[39] V. M. Yarsev, Phys. Status Solidi B **112**, 279 (1982).

[40] H. Tajima, S. Kyoden, H. Mori, and S. Tanaka, Phys. Rev. B **62**, 9378 (2000).

[41] A. Paineli and A. Girlando, J. Chem. Phys. **84**, 5655 (1986).